



Cite this: *Lab Chip*, 2014, 14, 4362

A magnetic nanocomposite for biomimetic flow sensing

A. Alfadhel, B. Li, A. Zaher, O. Yassine and J. Kosel*

A magnetic nanocomposite has been implemented as artificial hair on a giant magnetoimpedance (GMI) thin-film sensor for flow sensing. The 500 μm long and 100 μm in diameter pillars are composed of iron nanowires incorporated in polydimethylsiloxane (PDMS). The nanowires' length and diameter are 6 μm and 35 nm, respectively. Upon fluid flow, the pillars are deflected, causing a change in the magnetic field at the GMI element and a corresponding change in impedance. The permanent magnetic behavior of the nanowires in combination with the GMI sensor and the high elasticity of the PDMS pillars result in a high-performance flow sensor with low power consumption and potential for remote detection. No additional magnetic field is required to magnetize the nanowires or bias the sensor, which simplifies miniaturization and integration in microsystems. At a power consumption of 31.6 μW , air flow rates up to 190 mm s^{-1} can be detected with a sensitivity of 24 $\text{m}\Omega (\text{mm})^{-1} \text{ s}$ and a resolution of 0.56 mm s^{-1} while the range for water flow is up to 7.8 mm s^{-1} with a sensitivity of 0.9 $\Omega (\text{mm})^{-1} \text{ s}$ and a resolution of 15 $\mu\text{m s}^{-1}$. When power consumption is reduced to as low as 80 nW a high resolution of 32 $\mu\text{m s}^{-1}$ is still maintained.

Received 16th July 2014,
Accepted 27th August 2014

DOI: 10.1039/c4lc00821a

www.rsc.org/loc

Introduction

Cilia are micro-scale, hair-like structures that exist in nature and extend from the organism's cells. Taking fish as an example, their hair cells assist in performing a variety of functions such as preying or avoiding danger. When the cilia are exposed to a change in the fluid flow, they bend and transmit a signal to the organism. This signal is then translated into a specific function.

Recently, artificial cilia have been developed that could be used for various applications such as cell mechanics study,^{1,2} microfluidic propulsion,^{3,4} and flow sensing.⁵ For the hair flow sensors, different techniques such as thermal, piezoresistive, piezoelectric and magnetic have been utilized to detect cilia bending due to flow.⁵

A piezoresistive hair flow sensor realized by Chen *et al.* consists of a 600 μm by 80 μm vertical SU-8 hair-like structure fabricated by photolithography and a silicon resistor. The sensor was able to detect constant air flow between 0 m s^{-1} and 20 m s^{-1} with a resolution of 100 mm s^{-1} and water flow from 0 m s^{-1} to 0.4 m s^{-1} with a resolution of 5 mm s^{-1} . The sensor was also able to detect alternating flow velocity amplitudes down to the order of 0.7 mm s^{-1} in water at a frequency of 50 Hz.⁶

Flow sensors based on a vertical cilium and a strain gauge were developed by Liu. The study included two prototypes: silicon-based and polymer-based cilia. The silicon-based sensor was mounted on a glass plate and placed in a water tunnel with laminar flow. For water flows with velocities of 0 to 1 m s^{-1} , a resolution of 0.5 mm s^{-1} was reported. The response of the polymer-based sensor increases exponentially within the tested range, when applying air flow with velocities ranging from 0 m s^{-1} to 30 m s^{-1} . Liu concluded that silicon-based flow sensors showed higher sensitivity, whereas polymer-based sensors were more robust.⁷

Hein *et al.* proposed an inorganic nanocilia sensor based on magnetic nanowires (NWs) that utilizes the magnetic stray field of cobalt NWs for a biomimetic sensing approach. The NWs are mounted on a giant magneto-resistive sensor to detect their motion. The sensor has two possible applications: flow sensing and vibration sensing. Water flows were detected with velocities of 3.3 m s^{-1} to 40 m s^{-1} , a sensitivity of 0.55 $\mu\text{V (m)}^{-1} \text{ s}$ and a signal-to-noise ratio of 44, and vibrations in the low earthquake-like frequency range of 1 Hz to 5 Hz.⁸ The stiffness of the bare magnetic NWs prevents the measurement of low flow velocities. Nanocilia made of metals such as Co have a high possibility of corrosion, limiting their use for applications in, *e.g.*, microfluidic devices. Magnetic polymer cilia have also been realized using super-paramagnetic nanoparticles embedded in thin polymer films for various applications.^{3,9} This approach requires the application of rather large magnetic fields. For instance, Khaderi *et al.* applied a rotational magnetic field of 115 mT

Computer, Electrical and Mathematical Sciences and Engineering Division (CEMSE), King Abdullah University of Science and Technology (KAUST), Thuwal 23955, Saudi Arabia. E-mail: ahmed.fadhel@kaust.edu.sa

in amplitude and Digabel *et al.* used a $23 \times 10^3 \text{ T m}^{-1}$ magnetic field gradient to actuate the cilia. A favorable property of magnetic cilia is the absence of an electric contact and the possibility of remote detection or actuation.¹⁰

Recently, there has been great interest in developing sensors with low power consumption. However, reducing the power consumption usually leads to a reduction in the resolution. For example, a low-power thermal flow sensor developed by Cubukcu *et al.* shows a resolution below 10 mm s^{-1} at $177 \text{ } \mu\text{W}$.¹¹ High-resolution thermal flow sensors have a power consumption of more than 1 mW .¹² In this regard, hair flow sensors are attractive options and have been shown to operate at a power consumption as low as $140 \text{ } \mu\text{W}$ providing a resolution of 0.9 m s^{-1} .⁸

In this work, we describe a magnetic polymer hair flow sensor that provides both a high resolution and a very low power consumption. The sensor is composed of cylindrical polydimethylsiloxane (PDMS) pillars containing iron NWs and implemented on a giant magnetoimpedance (GMI) thin film sensor, which was chosen for its simple and cheap fabrication,¹³ high sensitivity^{13,14} and potential for wireless operation.¹⁵ The high elasticity of the magnetic-PDMS composite¹⁶ enables the detection of extremely low flow velocities. These advantages, together with its good resistance to corrosion, make the proposed hair flow sensor suitable for many applications.

Methods

1. Concept

The flow sensor is composed of eight PDMS pillars that are $500 \text{ } \mu\text{m}$ long and $100 \text{ } \mu\text{m}$ in diameter and have iron NWs $6 \text{ } \mu\text{m}$ in length and 35 nm in diameter incorporated. The magnetic nanocomposite pillars are fabricated on top of a GMI sensor (Fig. 1). The operating principle of the flow sensor is based on detecting the change in the magnetic field created by the permanent magnetic NWs, of the magnetic-PDMS pillars, when deflected by a fluid flow. A multi-layer GMI sensor, which offers a good compromise between sensitivity¹⁷ and fabrication complexity, is utilized to measure the change in the magnetic field. At small bias fields and at high operating frequencies, the impedance of GMI sensors is sensitive to external magnetic fields due to the strong dependence of the skin effect on magnetic permeability. A distinct advantage of this flow sensor is the permanent magnetic behavior of the iron NWs in the nanocomposite pillars, remedying the need for an external magnetic field to magnetize the pillars or bias in the GMI sensor. At resting position, the stray field of the pillars affects the GMI sensor with an average magnetic field value $H(0)$ that biases the sensor and changes its initial impedance. In the presence of a fluid flow, the pillars bend in the flow's direction. This bending results in a change in the stray field of the pillars with an average magnetic field value $H(\delta)$ affecting the GMI sensor, and hence changing its impedance.

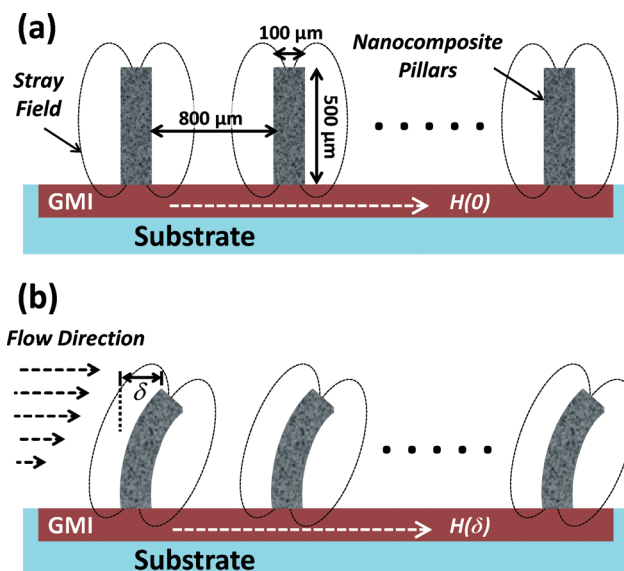


Fig. 1 Illustration of the flow sensor operation principle. (a) A GMI sensor is used to detect the stray field of the magnetic nanocomposite pillars, which is, on average, $H(0)$ without fluid flow. (b) Fluid flow causes the pillars to bend (δ is the tip deflection) changing the average magnetic field to $H(\delta)$.

The flow signal is obtained as the impedance change ΔZ , which is the difference between the GMI sensor's impedance Z_δ , when a flow is applied and the pillars' tips are deflected by δ , and the initial impedance Z_0 , when no flow is applied and $\delta = 0$. The impedance can be calculated from the average magnetic field value at the GMI sensor and the sensitivity of the GMI sensor S_{GMI} , which is assumed to be constant about the operation point. The sensitivity S of the flow sensor is the change in impedance over the average flow velocity $v_{\text{avg}}(\delta)$:

$$S = \frac{\Delta Z}{v_{\text{avg}}(\delta)} = \frac{Z_\delta - Z_0}{v_{\text{avg}}(\delta)} = \frac{S_{\text{GMI}}[H(\delta) - H(0)]}{v_{\text{avg}}(\delta)} \quad (1)$$

Using S together with the maximum impedance fluctuation Z_f (noise), the resolution is:

$$R = Z_f / S \quad (2)$$

The velocity inside the fluidic channel for a laminar flow is not constant but changes across the cross section area of the channel. The velocity is highest along the center of the channel and is decreasing toward the channel walls. The average flow velocity v_{avg} is estimated to be one half of the maximum flow velocity.¹⁸

Using the displacement-force relationship of an elastic cylindrical beam, the value of δ can be expressed for uniformly distributed forces F along the length of the pillar as:¹⁹

$$\delta = \frac{64}{3} F \frac{l^3}{\pi E D^4} = \frac{64}{3} \left(\frac{1}{2} \rho v_{\text{avg}}(\delta)^2 C_D A(\delta) \right) \frac{l^3}{\pi E D^4} \quad (3)$$

where l , E , and D are the length, the Young's modulus and the diameter of the pillars, respectively. The force is

proportional to the fluid density ρ , drag coefficient C_D and the area of the pillars that is facing the flow $A(\delta)$, which is a function of δ , since the effective area decreases as the pillars bend. C_D is computed using:²⁰

$$C_D = 0.8 + \frac{13.6}{\text{Re}} = 0.8 + \left(\frac{13.6\mu}{\rho v_{\text{avg}}(\delta) D_h} \right) \quad (4)$$

where Re is the Reynolds number, D_h is the hydraulic diameter and μ is the fluid dynamic viscosity.

Besides its advantages such as chemical resistance, PDMS is specifically chosen for its low Young's modulus value, making the pillars highly elastic and easy to bend at small flow velocities.

2. Fabrication

The 8 mm long and 400 μm wide multi-layer GMI sensor is composed of a 200 nm thick Cu layer sandwiched between two 100 nm thick $\text{Ni}_{80}\text{Fe}_{20}$ layers. The materials are deposited onto a glass substrate by e-beam evaporation with a constant magnetic field of 100 Oe applied in the transverse direction to induce a uniaxial magnetic anisotropy, creating a magnetically sensitive axis in the longitudinal direction. The sensor is patterned by a lift-off process (Fig. 2a).

Iron NWs are fabricated by electrodeposition in nanoporous aluminum oxide prepared by a two-step anodization process using oxalic acid on an aluminum substrate.²¹ Iron is chosen for its high magnetization at remanence and high coercivity, creating a large stray field and making the pillars difficult to demagnetize. Moreover, iron NWs have been shown to be biocompatible,²² and can be efficiently fabricated using this process with a high control of the properties.

The nanocomposite pillars are fabricated using a 500 μm thick poly(methyl methacrylate) (PMMA) master mold into which an array of eight holes, separated by 800 μm and each having 100 μm in diameter, is patterned with a CO_2 laser cutter (Universal PLS6.75). The nanocomposite is prepared by

mixing iron NWs with PDMS (Sylgard 184 Silicone Elastomer, Dow Corning Corporation) that is used as the polymeric matrix with an 18% NW-to-PDMS volume ratio. This ratio is sufficient to provide the biasing field for the GMI sensor; yet, it does neither adversely affect the polymerization process of PDMS nor the elasticity of the pillars. The composite is casted onto the surface of the substrate and the master mold is mounted on top of it such that the pillars are aligned along the GMI sensor (Fig. 2b, c). This structure is then placed in a desiccator for 30 minutes to remove any trapped air bubbles and assist in filling the pores. Next, the composite is cured at 90 $^\circ\text{C}$ for 1 hour, forming the pillars on top of the GMI sensor's surface. After releasing the cured pillars, they are fully magnetized by applying a magnetic field of 10 kOe.

The flow sensor is tested inside a fluidic channel, which is 1 mm high, 10 mm wide and 15 mm long and has an inlet and an outlet (Fig. 2d). The channel is fabricated with the laser cutter using three layers of PMMA substrates bonded by applying chloroform at the bonding joints and pressing the substrates by hand. The channel is then bonded to the sensor's substrate using an instant room temperature curing adhesive. The channel provides a small value of Re to avoid turbulence and achieve laminar flow.

The fabricated nanocomposite pillars on the GMI sensor are shown in Fig. 3. The bottom diameter of the pillars is slightly wider than the top diameter, which is a result of patterning the mold with the laser beam.

3. Characterization

Since a high elasticity of the nanocomposite pillars is crucial for a high sensitivity, the influence of the NWs on the Young's modulus is evaluated by applying a constant force of 0.5 N to a 2 cm long, 1 cm wide and 500 μm thick PDMS sample with 18% NWs. The nanocomposite has a Young's modulus of 270 kPa, which is only a slightly higher value than the 255 kPa found for a pure PDMS sample prepared under the same conditions. Hence, the advantage of the high elasticity of PDMS is maintained.

In order to test the magnetic properties, the magnetization curves along the length of the pillars and along the perpendicular direction are obtained using a vibrating sample magnetometer. As shown in Fig. 4, the nanocomposite pillars have a remanent magnetization of 2.1 memu and a

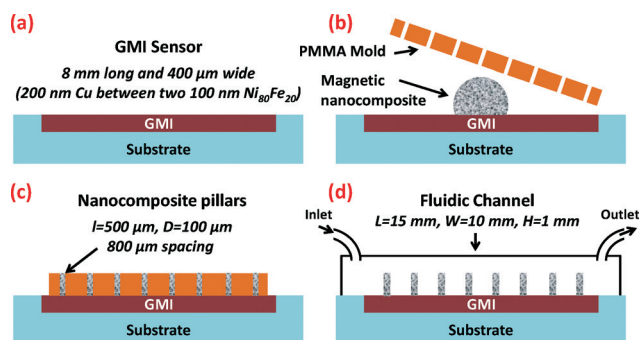


Fig. 2 Illustration of the flow sensor fabrication process. (a) A GMI sensor fabricated on a glass substrate. (b) A nanocomposite consisting of PDMS and magnetic NWs is placed on the substrate, and (c) a PMMA mold is mounted onto the composite. Then, the composite is cured at 90 $^\circ\text{C}$ for 1 hour. (d) The PMMA mold is removed, and the sensor is integrated into a PMMA fluidic channel.

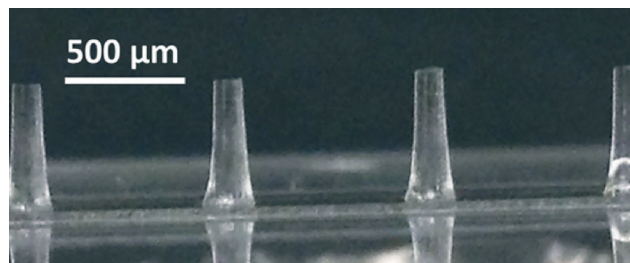


Fig. 3 Optical image of the fabricated nanocomposite pillars that are 500 μm in length and 100 μm in diameter.

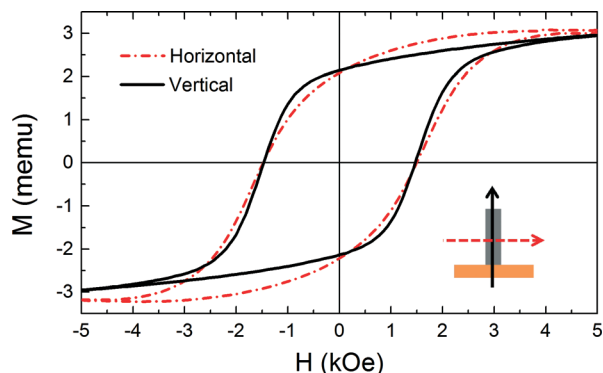


Fig. 4 Nanocomposite pillars' magnetization M as a function of applied field H obtained with a vibrating sample magnetometer in the vertical and horizontal direction with respect to the pillars' axes.

remanence-to-saturation magnetization ratio of 0.7 with a coercivity of 1520 Oe. The similarity of the magnetization curves in the vertical and horizontal directions indicates that the NWs are not fully aligned in a specific direction in the composite, with the vertical direction being slightly preferred. Electron microscopy images show the distribution of the NWs inside the pillars (Fig. 5a) and are used to determine the length of the NWs (Fig. 5b). X-ray diffraction analysis reveals that the NWs are polycrystalline iron with a thin shell of magnetite around the NWs (Fig. 6).

Iron NWs can be easily oxidized when exposed to a humid environment reducing the magnetization of the NWs. In order to study this effect, the remanent magnetizations of a nanocomposite exposed to air and a nanocomposite kept in water are measured over a period of 60 days (Fig. 7). The magnetization decreases over time at a reducing rate. The sample exposed to air retains 81% of the initial magnetization while the sample kept in water retains 76% of the initial magnetization. NWs inside the composite were oxidized due to the fact that PDMS is permeable to water molecules. This

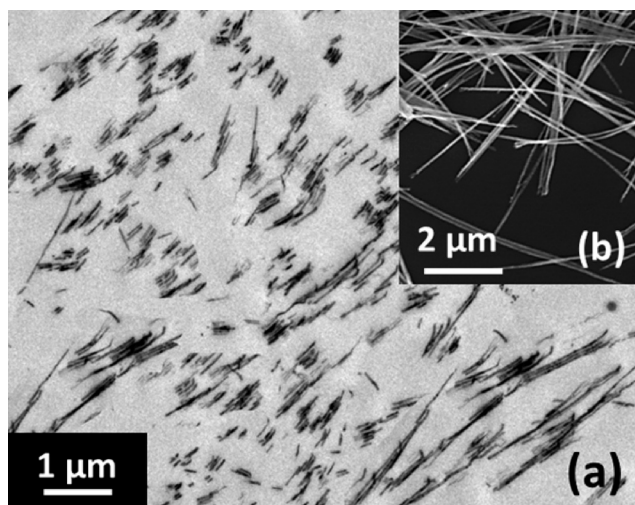


Fig. 5 (a) Transmission electron microscope cross-sectional image of a nanocomposite pillar. (b) Scanning electron microscope image of 6 μm long and 35 nm in diameter iron nanowires.

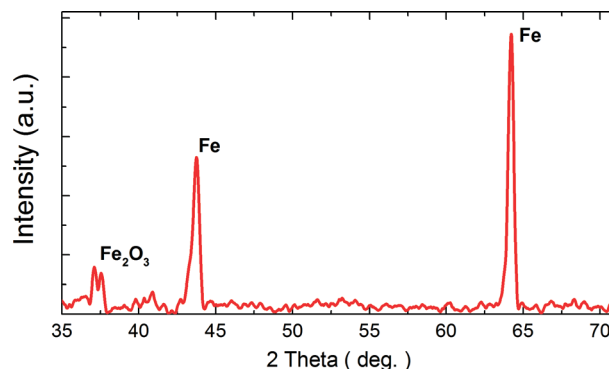


Fig. 6 X-ray diffraction results for iron nanowires.

explains the higher magnetization reduction rate for the sample kept in water. Fig. 7 also shows the remanent magnetizations of fully oxidized iron NWs that were oxidized by placing them in an oven for 24 hours at 150 °C. These NWs were oxidized forming magnetite as found by transmission electron microscopy. The magnetization of magnetite NWs is found to be 49% of that of iron NWs. This value is higher than the 30% reported in the literature,²³ which we attribute to an oxide layer around the NWs at the beginning of the experiment. Comparing the oxidation rate of the nanocomposites to that of bare iron NWs, Fig. 7 shows that the latter is oxidized with a much higher rate. After 10 days, the remanent magnetization of the bare wires in air decreases to 85% of the initial magnetization compared to the 98% and 92.5% of nanocomposite exposed to air and water, respectively.

Prior to testing the magnetic hair flow sensor, the GMI sensor is characterized in order to obtain the sensitivity S_{GMI} . Using a Helmholtz coil, a magnetic field of 0 Oe to 100 Oe with increments of 1 Oe is applied to the GMI sensor, and the impedance is obtained with an impedance analyzer (Agilent E4991A) at a current of 2 mA in amplitude and a frequency of 10 to 500 MHz (Fig. 8a). The GMI sensor response shows a peak at a field of 11 Oe corresponding to the anisotropy field of the $\text{Ni}_{80}\text{Fe}_{20}$ thin film. The response of the GMI

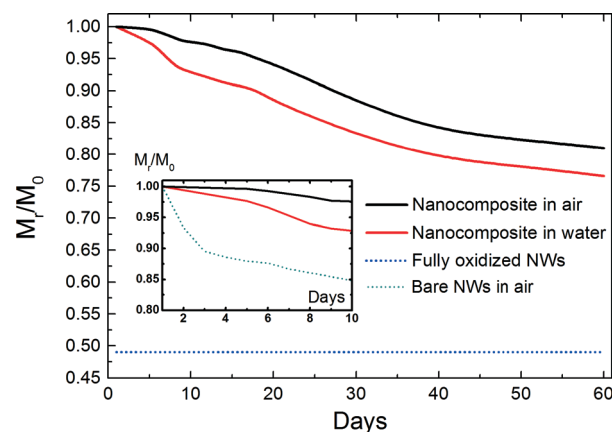


Fig. 7 Remanent magnetization M_r to initial remanent magnetization M_0 of nanocomposite pillars kept in air and water and of fully oxidized iron NWs. Inset: comparison between nanocomposites and bare iron NWs.

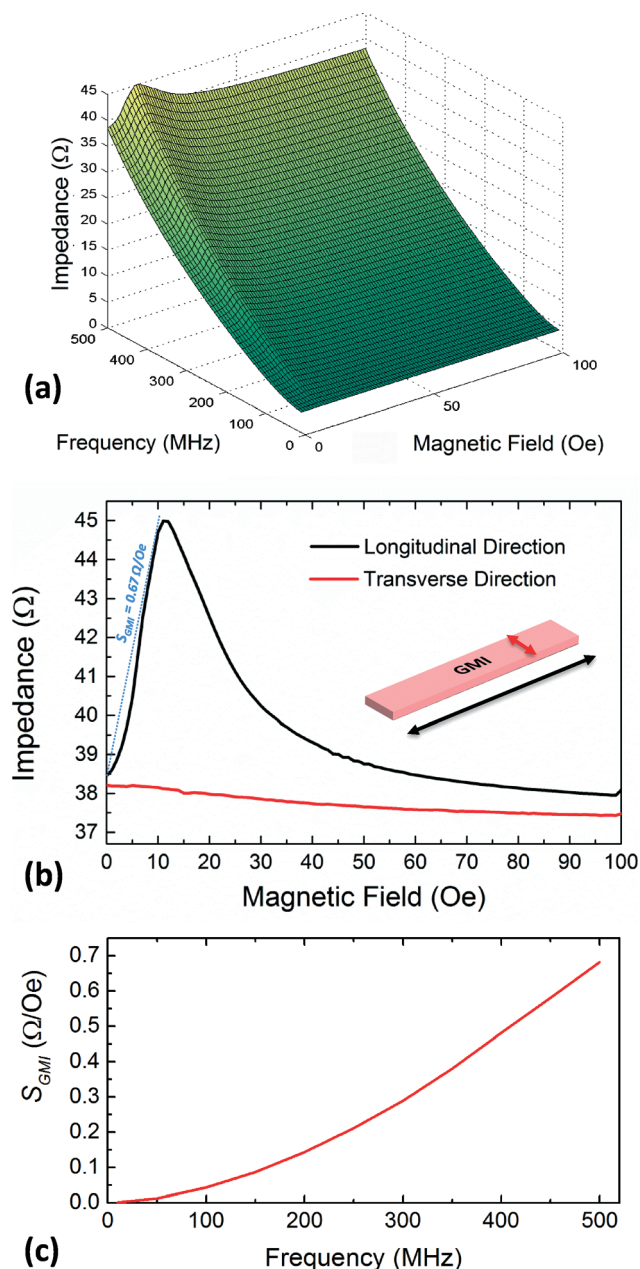


Fig. 8 (a) Impedance characterization of the GMI sensor as a function of the frequency and the magnetic field applied in the longitudinal direction. (b) Impedance response of the GMI sensor with external magnetic fields applied in the sensitive (longitudinal) and non-sensitive (transverse) directions at 500 MHz. The GMI sensor sensitivity S_{GMI} was determined by a linear fit. (c) S_{GMI} along the sensitive direction as a function of frequency.

sensor at 500 MHz and for fields applied in the longitudinal and transverse direction is shown in Fig. 8b. As can be seen, the GMI sensor is magnetically sensitive in the longitudinal direction while no significant impedance change is observed in the transverse direction. The GMI ratio, which is the maximum impedance change obtained with respect to the impedance at saturation field, is 20% and 1.3% in the longitudinal and transverse directions, respectively. This anisotropic magnetic property of the GMI sensor provides good selectivity in

terms of the direction of the magnetic signal that is being measured. The value of S_{GMI} is estimated through a linear fit of the GMI sensor's response between 0 Oe and 11 Oe, as shown in Fig. 8b, which includes the operating range within which the magnetic fields vary with the deflection. S_{GMI} increases with increasing frequency (Fig. 8c), therefore, 500 MHz is selected as the operating frequency, where S_{GMI} is $0.67 \Omega \text{ Oe}^{-1}$.

The flow sensor is tested by applying air and water volumetric flow rates using a syringe pump through a channel inlet in both sensitive and non-sensitive directions of the GMI sensor. The average flow velocity is calculated by dividing the applied volumetric flow rate by the channel cross-sectional area of 10 mm^2 . The impedance magnitude of the GMI sensor is measured with the impedance analyzer at a current of 2 mA in amplitude and a frequency of 500 MHz. A set of 10 data points at every flow velocity value is recorded over a period of 30 seconds. The values for Z_δ and Z_t are obtained from the average value and the maximum deviation from the average value, respectively. The current dependence of the flow sensor is tested for current amplitudes between 0.1 and 10 mA, which are the limits of the impedance analyzer. The experimental setup is shown in Fig. 9.

4. Computational model

The response of the flow sensor is computed from eqn (1) and eqn (3) using a Young's modulus of 270 kPa, a remanent magnetization of 2.1 memu and an S_{GMI} of $0.67 \Omega \text{ Oe}^{-1}$. The eight pillars are modeled by finite element simulations using commercial software (COMSOL) as 3D cylindrical beams in order to study the magnetic fields affecting the GMI sensor upon the deflection of the nanocomposite pillars. The magnetic NWs are accounted for by assigning flux density vectors to the pillars, which are calculated from the NWs' remanence value and the amount of NWs in the pillars. Fluid flow is simulated by rotating the pillars about the anchor point by an angle θ , which is related to the deflection by:

$$\delta = l \sin(\theta) \quad (5)$$

This changes the effective area of the pillar that is facing the flow to:

$$A(\theta) = \frac{\pi D}{2} l \cos(\theta) \quad (6)$$

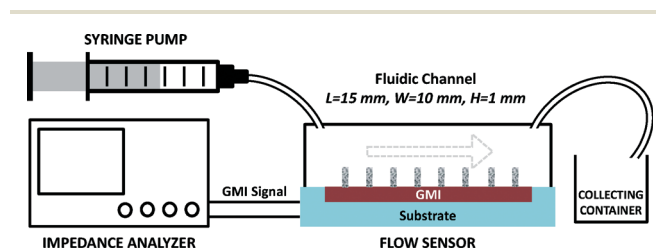


Fig. 9 Flow sensor experimental setup.

The average value of the magnetic field at the GMI sensor is:

$$H(\theta) = \frac{1}{n} \sum_{i=1}^n (H_x)_i \quad (7)$$

where H_x is the component of the magnetic vector field along the GMI sensor's sensitive direction, i is the summation index and n is the number of magnetic vectors used in the averaging process. The average magnitude of the magnetic field is calculated as:

$$H_{\text{mag}}(\theta) = \frac{1}{n} \sum_{i=1}^n (\sqrt{H_x^2})_i \quad (8)$$

When the pillars are straight, an average magnetic vector field of 0 Oe is obtained, due to the symmetry of the stray field. However, the magnitude of the magnetic field in this case is 3.2 Oe, which can be considered as the bias field of the GMI sensor. As the pillars are deflected, the stray field at the GMI sensor increases on one side of the pillar and decreases on the other side, causing the average magnetic field value to increase. When the pillars are fully deflected, the magnetic field reaches an average value of 1.3 Oe.

$v_{\text{avg}}(\delta)$ is calculated by combining eqn (4) with eqn (3), where $A(\delta)$ can be derived from eqn (5) and eqn (6) as:

$$A(\delta) = \frac{\pi D}{2} \left(\frac{\delta}{\sin(\theta)} \right) \cos(\theta) = \frac{\pi D \delta}{2 \tan(\theta)} \quad (9)$$

The flow sensor's impedance change can now be calculated from eqn (1) by relating $H(\delta)$ to the corresponding $H(\theta)$ and using S_{GMI} from the experiment.

Results and discussion

The results of the flow experiments are shown in Fig. 10a for air and Fig. 10b for water. The sensor is sensitive to average air flow velocities of 0 to 190 mm s⁻¹ with maximum values of $S = 24 \text{ m}\Omega (\text{mm})^{-1} \text{ s}$ and $R = 0.56 \text{ mm s}^{-1}$. In the case of water, the sensor operates in the range of 0 to 7.8 mm s⁻¹ with maximum values of $S = 0.9 \Omega (\text{mm})^{-1} \text{ s}$ and $R = 15 \mu\text{m s}^{-1}$. The range of flow rates for water is lower than that for air, due to the higher density of water, causing larger forces to be exerted on the pillars. In both cases the response increases in a relatively linear manner ($\pm 5\%$) between 0 and 0.6 mm s⁻¹ for water flow and between 0 and 18 mm s⁻¹ for air flow, with the slopes representing the maximum sensitivity. Another linear region ($\pm 3\%$) is observed for water flow between 1.9 and 7.8 mm s⁻¹ with $S = 13.5 \text{ m}\Omega (\text{mm})^{-1} \text{ s}$, and between 40 and 190 mm s⁻¹ with $S = 0.7 \text{ m}\Omega (\text{mm})^{-1} \text{ s}$ for air. Complete bending of the pillars results in saturating the impedance change at 0.53 Ω and 0.54 Ω for air and water flows, respectively.

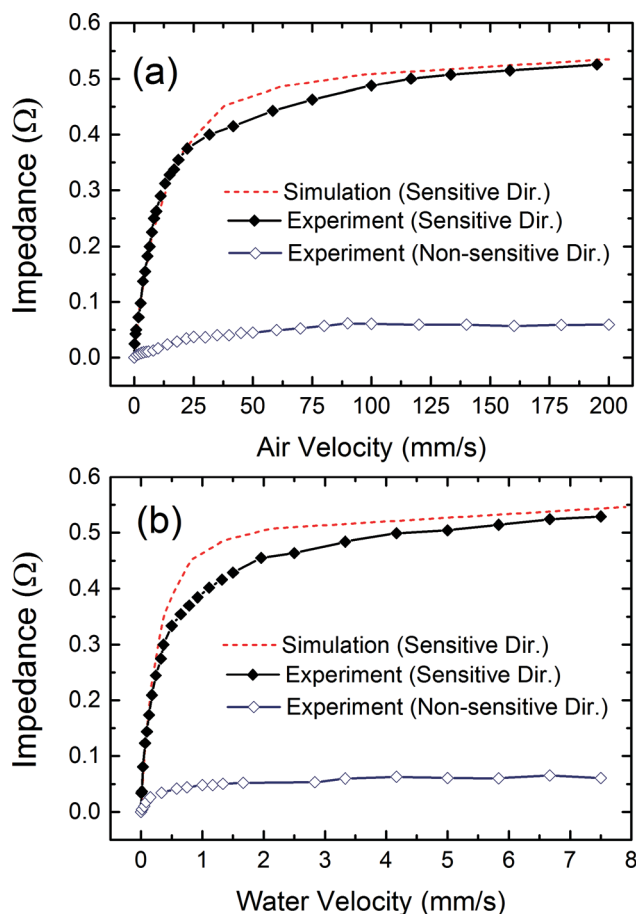


Fig. 10 Experimental and simulated impedance change of the flow sensor at different flow velocities along the GMI sensor's sensitive direction and non-sensitive direction for (a) air flow and (b) water flow.

The orientation of the fluidic channel with respect to the GMI sensor's alignment is changed in order to test the flow sensor along the non-sensitive direction. A smaller response of about 10% compared to the sensitive direction is obtained with saturation values of 0.059 Ω for air and 0.061 Ω for water.

Fig. 10 also shows the theoretical response of the flow, which is in close agreement with the experimental results. A slightly higher saturation value of 5.7 Ω is obtained from the theoretical model. This is most likely due to the actual magnetization of the pillars being lower than expected, indicating a lower NW concentration than expected. Theoretical impedance values at the knee region, which corresponds to around 70° pillar deflection, are higher than the experimental values, due to the assumption of rotation of straight pillars rather than their bending and neglecting the fact that the actual flow velocity inside the channel is decreasing toward the channel walls.

The performance of the flow sensor can be modified easily by changing the mechanical parameters of the pillars. Changing the diameter of the pillars, for example, leads to a different operating range, resolution and sensitivity (Fig. 11).

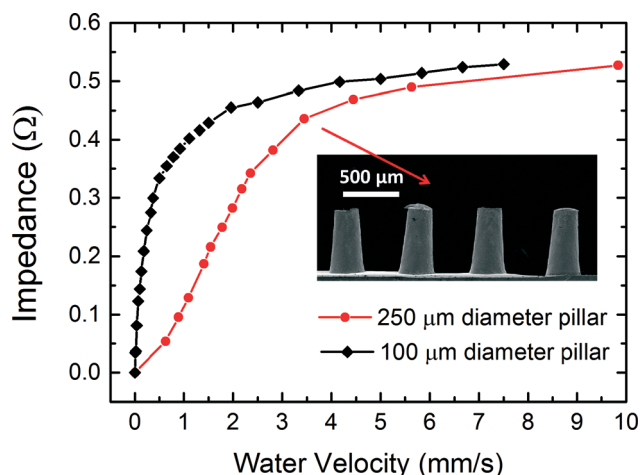


Fig. 11 Experimental impedance change of flow sensors with pillars of 100 μm and 250 μm in diameter and 500 μm in length at different flow velocities along the GMI sensor's sensitive direction for water flow. The fabricated pillars 250 μm in diameter are shown in the inset.

To demonstrate this point, a flow sensor is fabricated with 500 μm long and 250 μm in diameter nanocomposite pillars that have the same iron NW volume as the 100 μm pillars. The modified sensor operates in the range of 0 to 12 mm s^{-1} with maximum values of $S = 0.17 \Omega (\text{mm})^{-1} \text{ s}$ and $R = 79 \mu\text{m s}^{-1}$.

The average power consumption of the flow sensor, when operated at 2 mA current amplitude, is 31.6 μW . Power consumption can be further reduced by operating the sensor at lower current amplitudes. The current dependence of the flow sensor is shown in Fig. 12. As can be seen, there is almost no influence of the current on the measured impedance value with slightly higher values obtained at low current amplitudes. The impedance of the GMI sensor at 2 mA driving current has fluctuations $Z_f = 0.0135 \Omega$, while $Z_f = 0.0292 \Omega$ and $Z_f = 0.0096 \Omega$ at 0.1 mA and 10 mA, respectively. This indicates that the signal stability can be enhanced by increasing the driving current and hence increasing the resolution at the expense of power consumption. The operation at 10 mA leads to a slightly improved resolution of $10 \mu\text{m s}^{-1}$ at a power consumption of 790 μW . When

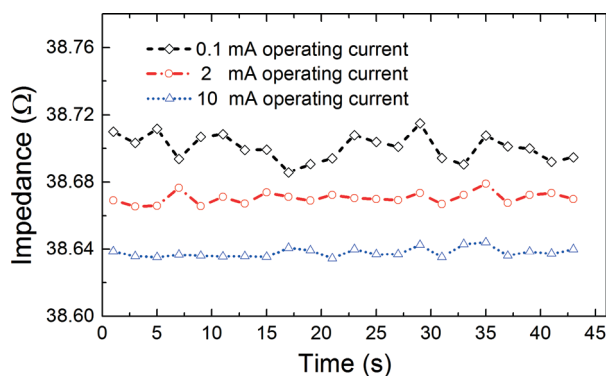


Fig. 12 Flow sensor impedance fluctuation over time for different current amplitudes.

operated at 0.1 mA, power consumption can be reduced to as low as 80 nW with the resolution still being $32 \mu\text{m s}^{-1}$.

Conclusion

Natural cilia are mimicked by nanocomposite pillars consisting of PDMS polymer with embedded iron nanowires. The pillars are permanent magnetic and have a high elasticity. They are integrated on a GMI thin-film sensor to detect the change in the pillars' stray fields, resulting from their bending upon the application of fluid flow. The flow sensor can be used for both water and air flow measurement applications and has an operating range in the case of air flow between 0 and 190 mm s^{-1} , with a sensitivity of up to $24 \text{ m}\Omega (\text{mm})^{-1} \text{ s}$ and a resolution of 0.56 mm s^{-1} , and in the case of water flow the operating range is between 0 and 7.8 mm s^{-1} with a sensitivity of up to $0.9 \Omega (\text{mm})^{-1} \text{ s}$ and a resolution of $15 \mu\text{m s}^{-1}$. The achieved resolution is high compared to previously reported flow sensors,^{5–8,11,24} with a very low power consumption of 31.6 μW compared to reported thermal flow sensors with 177 μW (ref. 11) or hair flow sensors with 140 μW .⁸ Power consumption can even be reduced to 80 nW, with only a small decrease in the resolution of water flow to $32 \mu\text{m s}^{-1}$.

The magnetic NW-based flow sensor proposed by Hein *et al.* offers the advantage of extremely small dimensions but suffers from the possibility of corrosion and the high stiffness that prevents detection of low flow velocities.⁸ The developed magnetic nanocomposite flow sensor has a good corrosion resistance, is highly elastic, and uses a simple and cost-effective fabrication method compared with a conventional soft lithography process that demands templates to be prepared in specialized facilities with expensive consumables.

Eight pillars were used in the current sensor design, which were arranged in a manner allowing full deflection of each pillar without touching each other. This design provides an average signal over a length of 8 mm and can be readily adjusted to meet other requirements. This has been demonstrated by modifying the pillars' diameter from 100 μm to 250 μm , which increased the flow velocity range at the cost of sensitivity and resolution. The performance of the proposed hair flow sensor could be further improved by optimizing the sensitivity of the GMI sensor, which showed a rather small GMI ratio in our case. In general, other magnetic field sensors could also be used such as contemporary magnetic tunnel junctions that might offer certain advantages over the GMI sensor. The advantage of the GMI sensor is its simple fabrication, robustness and the possibility to integrate the sensor with RF transducers for wireless operation, which could be useful for specific applications.

References

- 1 N. J. Sniadecki, A. Anguelouch, M. T. Yang, C. M. Lamb, Z. Liu, S. B. Kirschner, Y. Liu, D. H. Reich and C. S. Chen, *Proc. Natl. Acad. Sci. U. S. A.*, 2007, **104**, 14553.

- 2 A. Ghanbari, V. Nock, S. Johari, R. Blaikie, X. Chen and W. Wang, *J. Micromech. Microeng.*, 2012, **22**, 10.
- 3 S. N. Khaderi, C. B. Craus, J. Hussong, N. Schorr, J. Belardi, J. Westerweel, O. Prucker, J. R  he, M. J. Toonder and P. R. Onck, *Lab Chip*, 2011, **11**, 2002.
- 4 F. Fahrni, M. J. Prins and L. IJzendoorn, *Lab Chip*, 2009, **9**, 3413.
- 5 J. Tao and X. Yu, *Smart Mater. Struct.*, 2012, **21**, 113001.
- 6 N. Chen, C. Tucker, J. Engel, C. Yang, S. Pandya and C. Liu, *J. Microelectromech. Syst.*, 2007, **16**, 999.
- 7 C. Liu, *Bioinspiration Biomimetics*, 2007, **2**, S162.
- 8 M. Hein, M. Maqableh, M. Delahunt, M. Tondra, A. Flatau, C. Shield and B. Stadler, *IEEE Trans. Magn.*, 2013, **49**, 191.
- 9 J. Digabel, N. Biais, J. Fresnais, J. Berret, P. Hersen and B. Ladoux, *Lab Chip*, 2011, **11**, 2630.
- 10 S. Traxler, J. Kosel, H. Pf  tzner, E. Kaniusas, L. Mehnen and I. Giouroudi, *Sens. Actuators, A*, 2008, **2**, 142.
- 11 A. S. Cubukcu, E. Zernickel, U. Buerklin and G. A. Urban, *Sens. Actuators, A*, 2010, **163**, 449.
- 12 J. Kuo, L. Yu and E. Meng, *Micromachines*, 2012, **3**, 550.
- 13 M. Phan and H. Peng, *Prog. Mater. Sci.*, 2008, **53**, 323.
- 14 L. V. Panina and K. Mohri, *Sens. Actuators, A*, 2000, **81**, 71.
- 15 B. Li, P. Salem, I. Giouroudi and J. Kosel, *J. Appl. Phys.*, 2012, **111**, 07E514.
- 16 K. Keshoju and L. Sun, *J. Appl. Phys.*, 2009, **105**, 023515.
- 17 B. Li and J. Kosel, *J. Appl. Phys.*, 2011, **109**, 07E519.
- 18 Y. Cengel and J. Cimbala, in *Fluid mechanics: Fundamentals and Applications*, McGraw-Hill, 2nd edn, 2010, ch. 8, vol. 1, pp. 321–342.
- 19 M. Yang, N. Sniadecki and C. Chen, *Adv. Mater.*, 2007, **19**, 3119.
- 20 Y. Cengel and J. Cimbala, in *Fluid mechanics: Fundamentals and Applications*, ed. Suzanne Jeans, McGraw-Hill, USA, 1st edn, 2006, ch. 11, vol. 1, pp. 561–578.
- 21 K. Nielsch, F. M  ller, A. P. Li and U. G  sele, *Adv. Mater.*, 2000, **12**, 582.
- 22 M. Song, W. Song, H. Bi, J. Wang, W. Wu, J. Sun and M. Yu, *Biomaterials*, 2010, **31**, 1509.
- 23 J. M. D. Coey, in *Magnetism and Magnetic Materials*, Cambridge University Press, UK, 2009, ch. 1, p. 8.
- 24 A. Dagamseh, C. M. Bruinink, H. Droogendijk, R. J. Wiegerink, T. S. Lammerink and G. Krijnen, *Proceedings of the 9th IEEE Sensors Conference*, Hawaii, USA, 2010.